Biochimica et Biophysica Acta 1837 (2014) 1769–1780

Contents lists available at ScienceDirect

Biochimica et Biophysica Acta

journal homepage: www.elsevier.com/locate/bbabio

Integration of energy and electron transfer processes in the photosynthetic membrane of *Rhodobacter sphaeroides*

Michaël L. Cartron [a], John D. Olsen [a], Melih Sener [b,c], Philip J. Jackson [a,d], Amanda A. Brindley [a], Pu Qian [a], Mark J. Dickman [d], Graham J. Leggett [e], Klaus Schulten [b,c], C. Neil Hunter [a,*]

[a] Department of Molecular Biology and Biotechnology, University of Sheffield, Sheffield S10 2TN, UK
[b] Beckman Institute for Advanced Science and Technology, University of Illinois at Urbana-Champaign, Urbana, IL 61801, USA
[c] Department of Physics, University of Illinois at Urbana-Champaign, Urbana, IL 61801, USA
[d] ChELSI Institute, Department of Chemical and Biological Engineering, University of Sheffield, Mappin Street, Sheffield S1 3JD, UK
[e] Department of Chemistry, University of Sheffield, Brook Hill, Sheffield S3 7HF, UK

ARTICLE INFO

Article history:
Received 30 September 2013
Received in revised form 3 February 2014
Accepted 5 February 2014
Available online 13 February 2014

Keywords:
Bacterial photosynthesis
Cytochrome bc_1
Atomic force microscopy
Electron microscopy
Quinone
Membrane modelling

ABSTRACT

Photosynthesis converts absorbed solar energy to a protonmotive force, which drives ATP synthesis. The membrane network of chlorophyll–protein complexes responsible for light absorption, photochemistry and quinol (QH_2) production has been mapped in the purple phototrophic bacterium *Rhodobacter* (*Rba.*) *sphaeroides* using atomic force microscopy (AFM), but the membrane location of the cytochrome bc_1 (cytbc_1) complexes that oxidise QH_2 to quinone (Q) to generate a protonmotive force is unknown. We labelled cytbc_1 complexes with gold nanobeads, each attached by a Histidine$_{10}$ (His_{10})-tag to the C-terminus of cytc_1. Electron microscopy (EM) of negatively stained chromatophore vesicles showed that the majority of the cytbc_1 complexes occur as dimers in the membrane. The cytbc_1 complexes appeared to be adjacent to reaction centre light-harvesting 1-PufX (RC–LH1–PufX) complexes, consistent with AFM topographs of a gold-labelled membrane. His-tagged cytbc_1 complexes were retrieved from chromatophores partially solubilised by detergent; RC–LH1–PufX complexes tended to co-purify with cytbc_1 whereas LH2 complexes became detached, consistent with clusters of cytbc_1 complexes close to RC–LH1–PufX arrays, but not with a fixed, stoichiometric cytbc_1–RC–LH1–PufX supercomplex. This information was combined with a quantitative mass spectrometry (MS) analysis of the RC, cytbc_1, ATP synthase, cytaa_3 and cytcbb_3 membrane protein complexes, to construct an atomic-level model of a chromatophore vesicle comprising 67 LH2 complexes, 11 LH1–RC–PufX dimers & 2 RC–LH1–PufX monomers, 4 cytbc_1 dimers and 2 ATP synthases. Simulation of the interconnected energy, electron and proton transfer processes showed a half-maximal ATP turnover rate for a light intensity equivalent to only 1% of bright sunlight. Thus, the photosystem architecture of the chromatophore is optimised for growth at low light intensities.

1. Introduction

Photosynthetically-driven cyclic electron transport requires two membrane-bound components in purple bacteria, the RC–LH1 core complex and the cytbc_1 complex. In many purple phototrophs energy is absorbed by a third complex, LH2, many copies of which form a peripheral antenna for absorbing and transferring excitation energy to the LH1 complex that surrounds the RC. Excitation of a special pair of bacteriochlorophylls (BChls) within the RC releases an electron that passes rapidly along a series of pigments until it arrives at an exchangeable quinone, Q_B. Successive excitations generate the two electrons necessary to convert the Q_B quinone to a quinol which then undocks from the RC and diffuses through the lipid bilayer to a cytbc_1 complex. Here, quinol molecules are oxidised, protons are discharged into the enclosed lumen of the photosynthetic membrane and cytochrome c_2, bound to the periplasmic surface of the cytbc_1 complex, is reduced. Repeated turnovers of this cyclic system are made possible by the membrane-extrinsic cytochrome c_2 and the membrane-intrinsic quinone/quinol (Q/QH_2) molecules, each shuttling between the RC–LH1 and cytbc_1 complexes [1]. The same principles, of light harvesting, photochemistry and Q/QH_2 traffic between the RC and a membrane-bound cytochrome complex, apply to most photosynthetic organisms. However, energy migration among LH complexes and Q/QH_2 traffic between RC–LH1 and cytbc_1 complexes have conflicting requirements; dense packing of RC–LH1 and LH2 complexes fosters rapid energy transfer, but hinders lateral diffusion of Q/QH_2, effectively weakening the linkage between

Abbreviations: AFM, atomic force microscopy; BChl(s), bacteriochlorophyll(s); cyt, cytochrome; MS, mass spectrometry; TFA, trifluoroacetic acid; Rba., Rhodobacter; LH, light-harvesting; PFT, PeakForce Tapping (AFM); RC, Reaction Centre; TEM, transmission electron microscopy; TM, Tapping Mode (AFM); NiNTA, nickel triacetic acid; His, Histidine; β-DDM, β-dodecyl maltoside; TDM, n-tetradecyl-β-D-maltopyranoside

* Corresponding author at: Tel.: +44 114 222 4191; fax: +44 114 222 2711.
E-mail address: c.n.hunter@sheffield.ac.uk (C. Neil Hunter).

http://dx.doi.org/10.1016/j.bbabio.2014.02.003
0005-2728/

RC photochemistry and QH_2 oxidation at the Q_o site of the cytbc_1 complex. This linkage has been studied using short flashes of light to initiate electron transfer and QH_2 formation, and conflicting models for cyclic electron flow arose from experiments using intracytoplasmic membrane vesicles ('chromatophores') from *Rba. sphaeroides*. Joliot et al. [2] proposed that the RC and cytbc_1 form a supercomplex whereas others, notably Crofts and co-workers [3], explained their results without invoking a fixed structural and functional relationship between RC and cytbc_1 complexes. These opposing concepts for the supramolecular organisation of photosynthetic membranes, derived from kinetic experiments, are equivalent to the 'solid state' and 'liquid state' models proposed by Rich [4].

More recently Comayras and co-workers used a kinetic approach to study the distribution of RCs and quinones in *Rba. sphaeroides*, and concluded that within a chromatophore membrane there are confined quinone domains associated with up to six RCs [5]. Direct structural evidence is now required to determine the membrane location of the cytbc_1 complex in *Rba. sphaeroides*. A previous atomic force microscopy (AFM) study of the *Rba. sphaeroides* photosynthetic membrane [6] showed that dimeric RC–LH1–PufX 'cores' are connected to large arrays of closely-packed LH2 complexes but cytbc_1 complexes were not detected; the cytbc_1 structure [7] shows that the cytoplasmically-exposed face has very little surface topology to aid its identification by AFM, and only the cytoplasmic side of the membrane is generally observed in such experiments. Here, we have used a combination of electron microscopy (EM) and AFM to identify cytbc_1 complexes and determine their location and aggregation state in a chromatophore vesicle. We overcame the membrane topology problem by attaching a $Histidine_{10}$ (His_{10})-tag to the C-terminus of cytc_1, which enabled labelling by Nanogold® beads functionalised with Ni-nitrilotriacetic acid (Ni-NTA) groups. Pulldown experiments were also used to examine cytbc_1–RC–LH1–PufX associations. This new mapping information, together with quantitative mass spectrometry and membrane modelling, has allowed computation of energy conversion efficiencies for an atomic-level chromatophore vesicle.

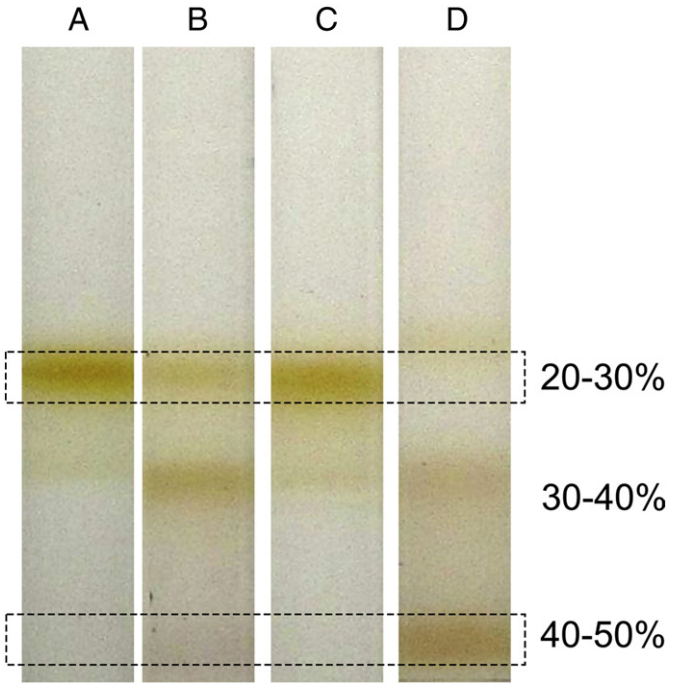

Fig. 1. Isolation of gold-labelled ICM vesicles on sucrose density gradients. Vesicles were treated with Ni-NTA-Nanogold® then fractionated on a 20%/30%/40%/50% (w/w) sucrose step gradient. A. Unlabelled wild-type vesicles at the 20–30% interface (upper box). B. wild-type vesicles labelled with Ni-NTA-Nanogold®. The vesicles migrate lower in the gradient due to unspecific gold labelling; the colouration at the 30–40% interface reflects the optical properties of the gold beads. C. Unlabelled His–cytbc_1 (strain BC1C10H) vesicles, D. BC1C10H vesicles labelled with Ni-NTA-Nanogold®; as a result of labelling the original membrane band is almost absent. The band at the 30–40% interface consists of partially-labelled vesicles. The lower box highlights the location of the specifically-labelled vesicles at the 40–50% interface. The gold beads confer a pink hue on the membranes.

2. Materials and methods

2.1. Growth of Rba. sphaeroides and conjugative transfer of pK18mobsacB

The strains used in this study were (1) *Rba. sphaeroides* 2.4.1 wild type, (2) *Rba. sphaeroides* BC1C10H (*fbcC*::thrombin-His_{10}), (3) *Escherichia* (*E.*) *coli* S17-1 [8], and (4) *E. coli* Rosetta II, pLysS (Novagen).

Single colonies of *Rba. sphaeroides* strains were inoculated into 10 ml of M22 + medium and grown for 48 hours at 34 °C in the dark with shaking, then 1 ml sub-cultured into 70 ml of M22 + in a 100 ml conical flask and incubated overnight at 34 °C with shaking. Further subculturing was used for growth under photosynthetic conditions in volumes up to 20 l.

The vector pK18mobsacB (ATCC® 87097™) was used to introduce the gene encoding the C-terminal His-tagged cytc_1 into the *Rba. sphaeroides* genome. The flanking regions of 1090 bp and 849 bp were made by PCR of genomic DNA using the primers listed below:

Primer 1: FbcC BamHI CGGGATCCTGACCTGGGTCGGCG
Primer 2: FbcC SacI GGGGAGAGCTCGTTCGTCTTCTTCTTGCCC
Primer 3: FbcC SalI GGTCGACGAGGACAGGCCCCGCTTC
Primer 4: FbcC HindIII CTGAAGCTTCTCGTCCAGCGGCTGATGG

pET52b + (Novagen) was used to provide the thrombin cleavage site and the 10-His tag which was introduced at the C-terminus of FbcC. The sequence of the C-terminal extension to cytc_1 was LALVPRGSSAHHHHHHHHHH. pK18mobsacB derivatives were transferred to *Rba. sphaeroides* using the conjugation-competent *E. coli* strain S17-1. Positive mutants were identified using colony PCR.

2.2. Membrane preparation

Cells harvested from a 2.5 l culture were resuspended in 30 ml of membrane buffer (20 mM MOPS, 600 mM NaCl, pH 7), a few grains of DNase I and lysosyme were added to the suspension and the cells were then disrupted in a French pressure cell at 18,000 psi; two cycles of French pressing were used to ensure the majority of cells were disrupted. The lysate was centrifuged at 15,000 rpm for 25 min, and the supernatant layered onto a discontinuous 15/40% (w/w) sucrose density gradient and centrifuged in a Beckman Ti45 rotor at 27,000 rpm (53,000 ×*g*) for 10 h. The chromatophore band, present just above the 15/40% interface, was collected with a micropipette then stored at 4 °C overnight or frozen at −20 °C until required.

2.3. Nanogold labelling of chromatophores and membrane patches

30 μl of A_{850} = 27 of chromatophores from the *Rba. sphaeroides* BC1C10His-tag mutant was incubated with 200 nM 5 nm Ni-NTA-Nanogold® (Nanoprobes); this concentration minimised a crosslinking effect, whereby Ni-NTA groups on a gold bead interact with more than one His-tagged cytbc_1 complex and promote formation of vesicle clusters. The membranes and gold beads were incubated in a 50 μl volume for up to 3 hours, then made up to 3 ml with buffer A (20 mM HEPES pH 7.5, 10 mM EDTA) and loaded onto a discontinuous 20%/30%/40%/50% (w/w) sucrose gradient in buffer A, and centrifuged in a Beckman SW41 rotor at 40,000 rpm for 4 hours. The nanogold-labelled bands, present just above the 40–50% interface (Fig. 1), were collected with a micropipette and immediately transferred onto carbon grids, as described above, for EM analysis.

The same procedure was adopted for labelling and isolation of nanogold-labelled membrane patches, except that after the initial 3-hour incubation β-dodecyl maltoside (β-DDM) was added to the mix to a final concentration of 0.1 mM, and incubated for an hour. The mix was then layered onto a discontinuous 20%/30%/40%/50% (w/w) sucrose gradient containing 0.025 mM TDM (n-tetradecyl-β-D-maltopyranoside; Anatrace, USA). The resultant patches were analysed by TEM and AFM.

2.4. Electron microscopy

Samples were applied to glow-discharged carbon coated copper grids and negatively stained with 0.75% w/v uranyl formate. Images were recorded at 100 kV on a Philips CM100 microscope equipped with a Gatan Ultrascan 667 CCD camera at 61,005× magnification.

2.5. Atomic force microscopy

Membrane patches were typically diluted 1:10 in 20 mM HEPES pH 7.5 before adding 5 μl of the diluted suspension to 45 μl of binding buffer, 20 mM HEPES pH 7.5, 150 mM KCl, 25 mM $MgCl_2$, on a freshly cleaved mica disc (Agar Scientific). The sample was incubated for ~1 hour at RT in a Petri dish with a piece of moistened paper towel to minimise drying. The binding buffer was removed with a pipette and the sample rinsed twice with 50 μl of imaging buffer, 20 mM HEPES pH 7.5, 100 mM KCl. SNL cantilevers, spring constant 0.24 N m^{-1}, resonant frequency 56 kHz (Bruker), were used in a Nanoscope Multimode 8 (Bruker) in Peakforce QNM imaging mode. Scan speeds were typically 1 Hz or less. The data were analysed and processed using NanoScope Analysis software (Bruker).

2.6. Progressive solubilisation of chromatophores and retrieval of His–cytbc_1 complexes on affinity columns

All steps were performed, as far as possible, at 4 °C. Approximately 60 ODU (@ 850 nm) of purified chromatophores in an end volume of 3 ml were used for each concentration of β-DDM (Glycon, Germany). A 10% β-DDM stock was made in buffer A (20 mM MOPS, 600 mM NaCl, pH 7) and the appropriate volume was slowly added to the membrane suspension to achieve final β-DDM concentrations of 0.1%, 0.5%, 1%, 2% and 2.5%. Following incubation at 4 °C with stirring for 40 minutes the samples were loaded onto individual Ni^{2+}-NTA columns (5 ml) equilibrated with buffer A. The columns were washed with 2 column volumes of Buffer A, then with sufficient Buffer B (20 mM MOPS, 600 mM NaCl, 20 mM imidazole, pH 7) until the flow-through was clear, typically 15 ml, and the sample eluted with buffer C (20 mM MOPS, 600 mM NaCl, 500 mM imidazole, pH 7). The final elution volume was typically around 3.5 ml, of which 200 μl was immediately transferred to a cuvette and absorbance spectroscopy performed as detailed in the next section. The remaining eluate was used for determination of protein and bacteriochlorophyll concentration, and for quinone and lipid extraction.

Three membrane samples were treated with 0.1, 0.5, 1.0, 2.0, or 2.5% β-DDM detergent, and the extracts fractionated using a total of 15 affinity columns. Each of the three eluates at a given starting detergent concentration was analysed for complexes or extracted for quinones and lipids in duplicate.

2.7. Absorbance spectroscopy

Absorbance spectra of purified chromatophore and membrane fractions were recorded on a Cary 50 UV-Vis spectrophotometer between 250 and 950 nm. When assessing the levels of the cytbc_1 complex the absorbance spectrum was recorded, then a few grains of sodium dithionite were added to reduce the samples, and the spectrum re-recorded. The extinction coefficients used were 7430 mM^{-1} cm^{-1} for the RC–LH1–PufX complex, 3720 mM^{-1} cm^{-1} for LH2 [18]. The concentrations of *b*- and *c*-type cytochromes were estimated using the extinction coefficients $\varepsilon_{561-575}$ of 22 mM^{-1} cm^{-1} and $\varepsilon_{551-540}$ of 19 mM^{-1} cm^{-1}, respectively [9]. Baselines were corrected and spectra were processed with Excel/Origin software as required.

2.8. Quinone and lipid extraction

All steps were performed as far as possible at 4 °C. Quinones and lipids were extracted following the same protocol. Eight volumes of 50/50 methanol/chloroform were added to one volume of untreated chromatophore vesicles. The mixture was vortexed several times and centrifuged, the colourless pellet was discarded and the coloured methanol/chloroform extract used for the lipid or quinone analysis. This procedure was repeated in triplicate for each sample solubilised with β-DDM.

2.8.1. Lipid analysis

Phospholipids were analysed and quantified according to [10]. All the extracted samples were dried into a glass tube to which was added 0.3 ml 70% perchloric acid, then the tubes were heated in a block for 3 h at 180 °C. 1 ml water, 0.4 ml 1.25 % (w/v) ammonium hepta-molybdate and 0.4 ml of 5% ascorbic acid were then added to each sample, vortexed and incubated for 5 minutes in a 100 °C water bath. The tubes were cooled in cold water (4 °C) before the absorbance was measured at 797 nm. Each sample was measured in triplicate. Individual phospholipids were separated by thin-layer chromatography and quantified as above, using published methods [11].

2.8.2. Quinone analysis

Quinones were analysed and quantified as described [12] with minor modifications. Quinones were extracted as described above. 50 μl of each sample was loaded unto an Ultrasphere ODS column (Beckman Coulter) and equilibrated with 100% methanol at a flow rate of 1 $ml.min^{-1}$. HPLC traces were analysed at 260, 270, 280, 290 and 300 nm and the areas under the peaks integrated. The column was calibrated with 5000, 2500, 1250, 625, 312.5, 156.25, 78.1, 39 and 19.5 $\mu g.ml^{-1}$ of coenzyme Q10 (Sigma) dissolved in 100% methanol.

2.9. Preparation of ^{15}N-labelled artificial protein standard

The ^{15}N-labelled internal standard was constructed as an artificial protein composed of concatenated tryptic peptide sequences [13,14] that are known to represent the target proteins in proteomic analysis. The N-terminal extension AWSWK was added to increase the absorbance of the artificial protein at 280 nm, thereby enhancing the accuracy of the quantification. The sequence was back-translated into the DNA sequence and optimised for expression in bacteria. The corresponding gene was synthesised (Bio Basic) with N-terminal *Nde*I and C-terminal *Bam*HI sites to enable sub-cloning into a pET14b vector (Novagen), incorporating an N-terminal His-tag sequence. *E. coli* (Rosetta II, *pLysS*, Novagen) was grown at 37 °C in 1.5 l M9 medium containing $(^{15}NH_4)_2SO_4$ (99 atom%, Cambridge Isotope Laboratories) to an OD of 0.7 at 600 nm. Overproduction of the protein was induced by the addition of 0.4 mM IPTG and the culture transferred to 20 °C for 16 hours. Cells were pelleted at 4000 ×*g* for 30 min at 4 °C and then re-suspended in 20 ml IMAC buffer (25 mM Tris/HCl pH 7.4, 300 mM NaCl, 5 mM imidazole). The cells were broken by sonication on ice in 10 × 30-second bursts and the insoluble fraction pelleted by centrifugation at 33,000 ×*g* for 30 min at 4 °C. The pellet was washed in IMAC buffer and re-centrifuged. The insoluble fraction was re-suspended in IMAC buffer containing 8 M urea and sonicated on ice in10 × 30-s bursts. The urea extract was stirred for 1 hour at 4 °C and clarified by centrifugation at 33,000 ×*g* for 30 minutes at 20 °C. The supernatant was applied to a 5 ml Ni^{2+}-charged chelating Sepharose column (GE Healthcare) equilibrated in IMAC buffer containing 8 M urea. The column was washed with 50 ml IMAC buffer containing 8 M urea followed by 50 ml IMAC buffer

containing 8 M urea and 50 mM imidazole. The ^{15}N-(His_6)-protein standard was eluted from the column with IMAC buffer containing 8 M urea and 250 mM imidazole and its concentration determined from the calculated molar extinction coefficient at 280 nm (www.expasy.org/protparam/).

2.10. Quantification of proteotypic peptides from subunits of the reaction centre, cytochrome bc_1, ATP synthase and terminal cytochrome c oxidases by liquid chromatography coupled to mass spectrometry

Chromatophores were buffer exchanged into 50 mM NH_4HCO_3, 0.1 mM DTT, 5 mM $MgCl_2$ using a PD-10 column (GE Healthcare) and the protein concentration determined at 1.39 mg/ml by Bradford assay. 0.2 ml membrane (278 μg) was mixed with 50 pmol ^{15}N-labelled artificial protein standard and 11 μg trypsin (proteomics grade, Sigma) in a total volume of 0.8 ml 0.05% ProteaseMax surfactant (Promega) in 50 mM NH_4HCO_3. Digestion was carried out at 48 °C [15] for 6 hours before transfer to 37 °C. 0.2 ml aliquots were removed at 3, 6 and 23 hours and immediately added to 20 μl 5% trifluoroacetic acid (TFA) to stop digestion and hydrolyse the surfactant. After incubation for 5 minutes at RT, samples were centrifuged at 16,000 ×*g* for 5 minutes and the supernatant applied to a C_{18} SpinTip (Protea Biosciences) according to the manufacturer's instructions. The eluted tryptic peptides were dried in a vacuum centrifuge, re-dissolved in 20 μl 0.1% TFA, 3% acetonitrile and 2 μl aliquots (equivalent to 6.95 μg membrane protein and 1.25 pmol ^{15}N-labelled protein standard) were analysed in duplicate by nanoflow liquid chromatography (Ultimate 3000 RSLCnano, Dionex) coupled to a Maxis UHR-TOF mass spectrometer (Bruker). Peptide separation was performed using 5 mm × 300 μm trapping and 150 mm × 75 μm analytical PepMap C_{18} reverse-phase columns (Dionex) with linear gradient elution from 4% solvent A (0.1% formic acid in water) to 40% solvent B (0.1% formic acid in 80% acetonitrile) over 90 minutes at 0.3 μl.min^{-1}. Mass spectra were acquired in profile mode with automatic dependent MS/MS scans.

The identities of the tryptic peptides, both unlabelled (from chromatophore) and ^{15}N-labelled (from the artificial protein standard) counterparts, were confirmed by searching the *Rba. sphaeroides* complete proteome database (ExPASy) using Mascot Server v. 2.2.01 (Matrix Science). DataAnalysis v. 4.0 software (Bruker) was used to extract ion chromatograms for the target peptide ions from the profile MS data and average the spectra across the relevant peaks. The averaged spectra were then processed to display the monoisotopic ion intensity values for each ^{14}N/^{15}N pair which enabled the quantification of these peptides (see Table S2).

2.11. Modelling chromatophore structure and function

Placement of light harvesting proteins LH2 and LH1-RC was performed as reported earlier [16,17] employing the area-preserving inverse-Mollweide transformation to map planar AFM images upon spherical domains and manually adjusting protein locations to remove steric clashes. The size and shape of the vesicle are observed by EM and AFM [18]. The packing density of LH2 domains for the intact vesicle was determined in a previous study [19]. The stacking pattern of RC–LH1–PufX dimers follows the curvature and association profiles observed earlier [17,20]. The relative spatial associations of cytbc_1 and ATP synthase complexes with respect to the LH proteins were determined in accordance with proteomics studies [21] as well as negative stain EM images (Figs. 2–4). The relative stoichiometry of proteins in the chromatophore was established through spectroscopy of the LH pigments [18] as well as from MS data (Table 1).

Electronic excitations that result from photon absorption are quickly delocalized over the pigment cluster of each LH protein. Thermal equilibrium of excited states within each pigment cluster is reached on timescales (<1 ps) that are shorter than excitation transfer between nearby proteins (~5–10 ps) [22]. Correspondingly, migration of excitation across pigment clusters is a Markovian process and can be described by the modified Förster formalism [23].

In this formalism, excited states of a pigment cluster I containing N_I pigments are described by an effective Hamiltonian [17]

$$H^I = \sum_{i=1}^{N_I} \varepsilon^I{}_i |i\rangle\langle i| + \sum_{i>j>0}^{N_I} V^I_{ij}(|i\rangle\langle j| + |j\rangle\langle i|) \quad , \tag{1}$$

where $|i\rangle$ are the Q_y-states of individual BChls forming a basis for H^I. The rate of excitation transfer between a donor pigment cluster D and an acceptor pigment cluster A is given by the modified Förster formula (see [23] for a review)

$$k_{DA} = \frac{2\pi}{\hbar} \sum_{m\in D} \sum_{n\in A} e^{-\beta\varepsilon_m} |\langle \tilde{n}|H_{DA}|\tilde{m}\rangle|^2 J_{mn} / \sum_{p\in D} e^{-\beta\varepsilon_p} \quad , \tag{2}$$

where $|\tilde{m}\rangle$ and $|\tilde{n}\rangle$ are the eigenstates for the effective Hamiltonians H^D and H^A, given by Eq. (1), corresponding to the donor and acceptor clusters, D and A, respectively; J_{mn} are spectral overlaps, in units of 1/energy, computed in [23,50]; ε_m are eigenvalues of H^D for pigment cluster D, given by $H^D|\tilde{m}\rangle = \varepsilon_m|\tilde{m}\rangle$ and H_{DA} is the matrix of cross-couplings between pigments of clusters D and A. Excitation transfer across the chromatophore is subsequently governed by a first order kinetics matrix κ constructed from the inter-cluster transfer rates k_{DA} according to

$$(\kappa)_{IJ} = k_{JI} - \delta_{IJ}\left(\sum_M k_{IM} + k_{diss} + k_{CS}\delta_{I,RC}\right) \quad , \tag{3}$$

where k_{diss} and k_{CS} denote the dissipation and the RC charge separation rates, respectively; $\delta_{I,RC} = 1$ if the pigment cluster I belongs to a RC and $\delta_{I,RC} = 0$ otherwise. The rate matrix κ has dimension N equal to the total number of pigment clusters in the network; these clusters involve the LH2, LH1 and RC pigments.

The quantum yield, q, of the chromatophore pigment network, defined as the probability of an absorbed photon to cause charge separation, can accordingly be expressed in terms of the matrix κ in Eq. (3) [17,23]

$$q = -k_{CS}\langle RC|\kappa^{-1}|0\rangle \quad , \tag{4}$$

where $|0\rangle$ denotes the N-dimensional vector of initial probabilities for the system and $|RC\rangle = \sum_I \delta_{I,RC}|I\rangle$. The quantum yield of $q = 0.91$ determined thus for the vesicle shown in Fig. 7A is consistent with earlier studies [16,17]. The quantum yield is computed for the chlorophyll network; photons absorbed by carotenoids are accounted for by the chlorophyll q value. Following excitation transfer, the quinols that are produced at the RC migrate to cytbc_1, which subsequently generates a proton-motive force to be utilized for ATP production at the ATP synthase.

In the following, the ATP turnover rate of the chromatophore under steady-state illumination is computed. This computation is achieved by relating the ATP production rate, $k_{ATP}(I)$, for a given illumination I to the quinol turnover in the chromatophore, which in turn is expressed in terms of the RC cycling time for quinones, $\tau_{RC}(I)$. The RC cycling time, $\tau_{RC}(I)$, is the mean time for the mobile quinone at the RC to be replaced upon conversion to quinol; $\tau_{RC}(I)$ depends on illumination and, through quinone diffusion dynamics, on the spatial arrangement of membrane proteins. The cycling time, $\tau_{RC}(I)$, acts as an important rate-determining constant of the system. It is prohibitive and also unnecessary to simulate the diffusion processes of the quinone/quinol in the chromatophore directly. Instead, the cycling time, $\tau_{RC}(I)$, is estimated from experimental observations [24]. Since spatial details and time dependence of quinone/quinol diffusion dynamics are not modelled, only steady state processes are considered below.

Bioenergetic processes other than ATP synthesis that utilize the proton-motive force, such as NADH/NADPH synthesis or motility,

are not considered. Therefore, the cytoplasmic state of the cell is not modelled directly, and the cytoplasm is assumed to function as a perfect sink instead. Accordingly, the ATP turnover rates estimated in this study should be viewed as upper limits.

For typical low-light intensities accessible to purple bacteria, quinol turnover and subsequent ATP production are rate-limited primarily by processes in cytbc_1 as suggested also by other studies [25]. In the following, rate limitation at the ATP synthase is not considered explicitly since the reported maximal ATP turnover rate of 270 ± 40 ATP/s per ATP synthase [26] far exceeds ATP turnover achievable through photosynthetic quinol turnover processes even at saturation light intensities. Rate limitation due to the proton or cytochrome c_2 pools are also considered irrelevant for typical growth conditions as the respective processes become limiting only at very high light intensities or for vesicles containing a much greater number of cytbc_1 complexes than observed.

Under steady state conditions, the rate with which closed (i.e. unavailable for excitation processing) RCs open (i.e. become ready again for receiving an excitation to initiate quinone photochemistry) must equal the rate with which open RCs close. Therefore, follows

$$\frac{1}{\tau_{RC}(I)}\left(n_{RC}-n_{RC}^{open}(I)\right)=\frac{1}{2}Iq\,p_{RC}(I)\ , \tag{5}$$

where $1/\tau_{RC}(I)$ is the rate with which closed RCs reopen; n_{RC} and $n_{RC}^{open}(I)$ denote the total number of RCs in the system and those that are open, respectively; q is given by Eq. (4); $p_{RC}(I)=n_{RC}^{open}(I)/n_{RC}$ is the fraction of RCs that are open; the prefactor 1/2 accounts for each quinol turnover requiring two electrons; the light intensity I is given in terms of photons absorbed by the system chlorophyll and carotenoids per second.

The probability for open RCs, $p_{RC}(I)$, can be related to the cycling time, $\tau_{RC}(I)$, using Eq. (5),

$$p_{RC}(I)=\left(1+\frac{1}{2}Iq\tau_{RC}(I)\frac{1}{n_{RC}}\right)^{-1}. \tag{6}$$

Since the cycling time, $\tau_{RC}(I)$, cannot be computed currently from a simulation of quinone diffusion processes, it is approximated below as an interpolation [27] between a low light limit, τ_L, and a high light limit, τ_H, adopted on the basis of experimental data. At the low light limit, where the quinone/quinol pool comprises almost entirely of quinones, a quinol departing the RC is replaced with a quinone from the immediate vicinity of the RC within time, τ_L, which is observed in low-light adapted LH2-rich chromatophores to be $\tau_L = 3$ ms [24]. At the high light limit, where the pool comprises mostly of quinols, the replacement rate of quinones at the RC is limited by the total quinol processing rate, $B=n_B{\tau_B}^{-1}$, at the n_B cytbc_1 dimeric complexes of the chromatophore, τ_B denoting the quinol turnover time at a dimeric cytbc_1 complex. The high light limit of the cycling time, τ_H, can be determined by observing that the total quinol turnover rates at the RCs and cytbc_1 complexes must balance for steady state illumination at large I, from which follows

$$\tau_H=\tau_B\frac{n_{RC}}{n_B}. \tag{7}$$

The probability, $pQ(I)$, that a cytbc_1 dimeric complex is involved in quinol turnover and is unavailable for further quinols, is given by $p_Q(I)=1-exp(-\frac{1}{2}Iq/B)$; the rate Iq corresponds to the maximal electron turnover rate at the RCs and the factor 1/2 accounts for every quinol requiring two electron transfers. Accordingly, the interpolation of the cycling time, $\tau_{RC}(I)$, between the low and high illumination values, τ_L and τ_H, respectively, is given by the formula

$$\tau_{RC}(I)=\tau_L+(\tau_H-\tau_L)\left(1-e^{-\frac{1}{2}IqB^{-1}}\right)\ . \tag{8}$$

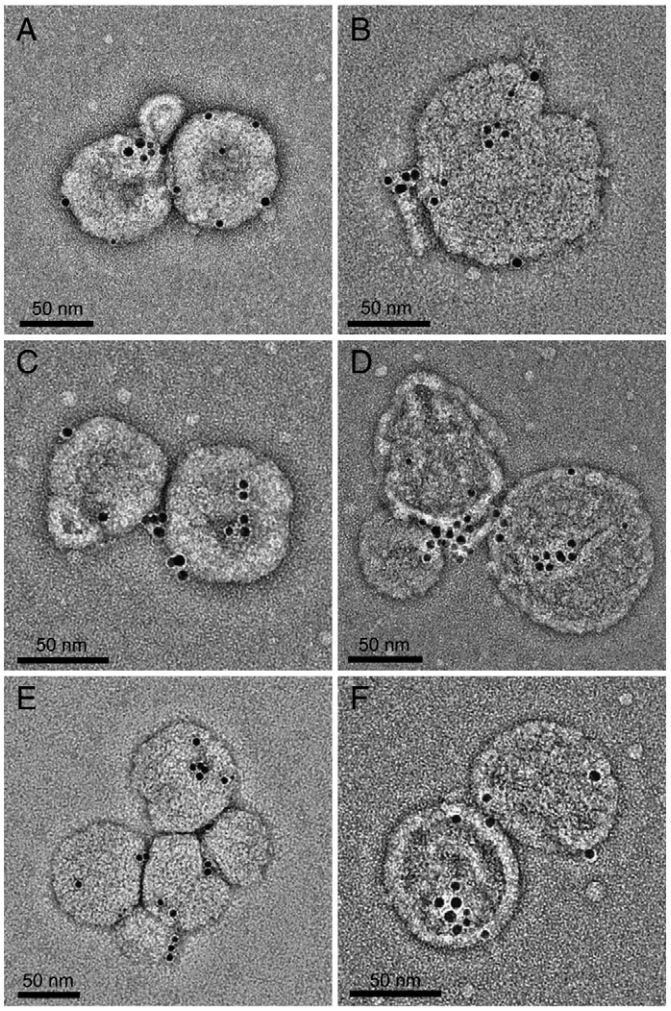

Fig. 2. Identification and membrane localisation of cytbc_1 complexes. A–F. Negatively stained whole chromatophores with cytbc_1 complexes labelled with gold NTA-Nanogold®. The edge-to-edge separation of pairs of gold beads is 2.4 ± 0.5 (S.D.) nm $n = 118$, compatible with the structure of the *Rba. sphaeroides* cytbc_1 dimer complex[12,13] and also the surface shell of the Ni-NTA nanoparticle.

One can finally express the ATP turnover rate, $k_{ATP}(I)$, in terms of the illumination I and the utilisation probability, $\eta_Q(I)$, for quinol turnover using Eqs. (6)–(8)

$$k_{ATP}(I)=\frac{1}{2}I\,\eta_Q(I)\ \ =\frac{1}{2}Iq\left(1+\frac{1}{2}Iq\tau_{RC}(I)\frac{1}{n_{RC}}\right)^{-1}, \tag{9}$$

where the prefactor 1/2 follows because the synthesis of one ATP requires the translocation of four protons and every electron cycled at a cytbc_1 dimeric complex translocates two protons. Here, the probability, $\eta_Q(I)=q\,p_{RC}(I)$, for an absorbed photon to be utilized for quinol turnover is the product of the probability for the photon to initiate charge transfer at a RC, namely q, given by Eq. (4), and the probability for the RC to be open, $p_{RC}(I)$, given by Eq. (6). The description in terms of Eqs. (5-8) is provided in more detail in a forthcoming publication.

3. Results

3.1. Site-directed gold labelling of cytbc_1 complexes in intact chromatophores, and their detection by electron microscopy and AFM

A gene encoding the C-terminal His-tagged cytc_1 was integrated into the *Rba. sphaeroides* genome, replacing the native cytc_1 (*fbcC*) gene and ensuring a native copy number for the tagged protein. The resulting

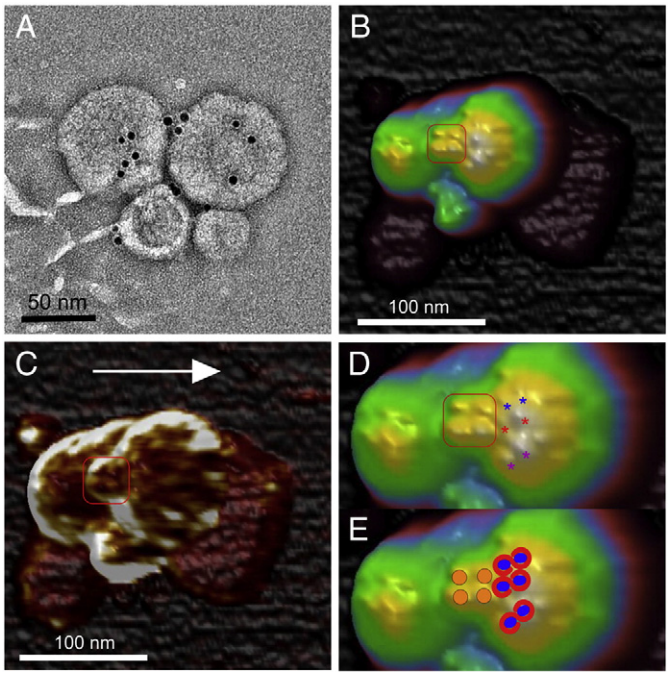

Fig. 3. EM and AFM analyses of intact chromatophores labelled with nanogold. A. Negative stain EM image of a cluster of nanogold-labelled chromatophores. B. False colour 3-D representation of AFM data of nanogold labelled chromatophores under liquid, filtered to reduce noise. The red box indicates four putative nanogold beads. The low lying features that extend from the cluster contain lipid without protein. The data were treated with a low pass filter to reduce noise. C. A 3D representation of the deformation channel data overlaid onto the height data in B. The red box denotes four zones of relatively low deformation; the white areas, which correspond to high deformation and are directed along the sides of the chromatophores in the scan direction (white arrow), show the highly flexible nature of the uncollapsed chromatophore. The data were treated with a low pass filter to reduce noise. D. Close-up of the image in B with pairs of coloured asterisks denoting the H-subunits of RC–LH1–PufX core complexes. E. Interpretation of the AFM data; the 9 nm separation of the peaks highlighted by the pairs of blue, red or magenta asterisks is consistent with the peak-to-peak separation of H-subunits in a RC–LH1–PufX dimer complex. The unknown topological features in the red box are indicated with orange circles.

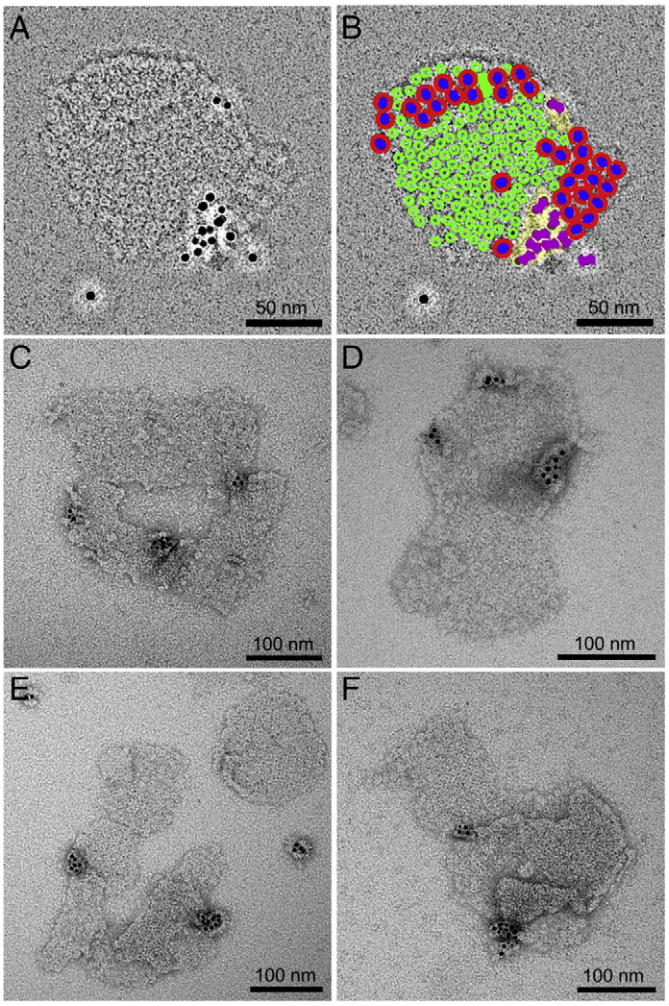

Fig. 4. Negatively stained membrane patches with cytbc_1 complexes labelled with gold NTA-Nanogold®. A. Patch consisting of one membrane bilayer with gold-labelled cytbc_1 complexes. B. Assignment of negatively stained features to LH2 complexes (green), RC–LH1–PufX complexes (red/blue) or cytbc_1 dimers (purple). C–F. A selection of other negative stained gold-labelled membrane patches showing evidence of LH2 and RC–LH1–PufX complexes.

strain, BC1C10H bearing a His_{10}-tag on the cytoplasmic face of cytc_1, grew photosynthetically at normal rates. Chromatophores were prepared from a photosynthetically grown culture of this strain were labelled with 5 nm Ni-NTA-gold beads in the absence of detergent, and fractionated on a sucrose step gradient as described in Materials and methods. Controls with either no gold label or no His-tag were also analysed (Fig. 1) and only gold-labelled BC1C10H vesicles produced a new band at the 40–50% interface, with the original membrane band at the 20%–30% step almost absent. Labelled chromatophores from the 40–50% fraction were negatively stained and analysed by EM. The images (Fig. 2A–F) show that the majority of the cytbc_1 complexes (nanogold edge-to-edge separation 2.4 ± 0.5 nm (S.D.) $n = 118$), occur as dimers in the membrane, consistent with the reported structure [7], and a recent kinetic study [28]. We used a nanogold concentration that minimised formation of vesicle clusters, which can be created by Ni-NTA groups on a gold bead interacting with His-tagged cytbc_1 complexes from different vesicles. Thus, only one half of a dimer might be labelled, giving apparent cytbc_1 monomers. Apparent monomers can also arise from one gold bead binding to both His-tags of the dimer, although the possibility of monomeric cytbc_1 complexes cannot be excluded. Another striking feature of these images is the tendency of cytbc_1 to form small clusters of two or more dimers.

The gold-labelled chromatophores harvested from the band at the 40–50% interface (Fig. 1, lane D) were also analysed by Peak Force Tapping AFM under liquid to attempt to identify protruding gold beads on the exposed cytoplasmic face of the chromatophore, as initially seen in EM (Figs. 2 and 3A). In Fig. 3 we compare an EM image of labelled chromatophores with a possibly interlinked pair of chromatophores adsorbed to mica and imaged by AFM; interlinked vesicles have been seen in cryo-EM of frozen sectioned cells [29]. Fig. 3A shows the typical circular appearance of native chromatophores when dried down upon a carbon film EM grid; the diameter is greater than that of a chromatophore under liquid as these vesicles collapse upon desiccation, forming appressed discs [29]. In the AFM image of chromatophores under liquid in Fig. 3B the maroon-coloured extensions are protein-free lipid zones, as judged by their ~4 nm height above the mica substrate (also see Fig S1). The vesicles, which appear to be connected, are ~26 and ~30 nm high (see the section in Fig. S1A), similar to previous AFM measurements of isolated WT chromatophores of 37.6 ± 4.1 nm [19]; the smaller height here could indicate partial flattening of the chromatophores.

Discrete raised topology can be seen on the upper surfaces in Fig. 3B and one particular region of four similar height features is outlined by the red box on the right-hand vesicle. These paired, regular features give a low deformation signal (Fig. 3C, red box), in comparison with the white areas of the chromatophores where the AFM tip (the direction of the scan is shown by the white arrow) pushes into the vesicle side producing a high deformation signal. These four topological features (Fig. 3C, red box) are tentatively assigned to NiNTA functionalised gold beads attached to cytbc_1 dimers. This cluster lies adjacent to the more closely spaced features denoted by pairs of coloured asterisks

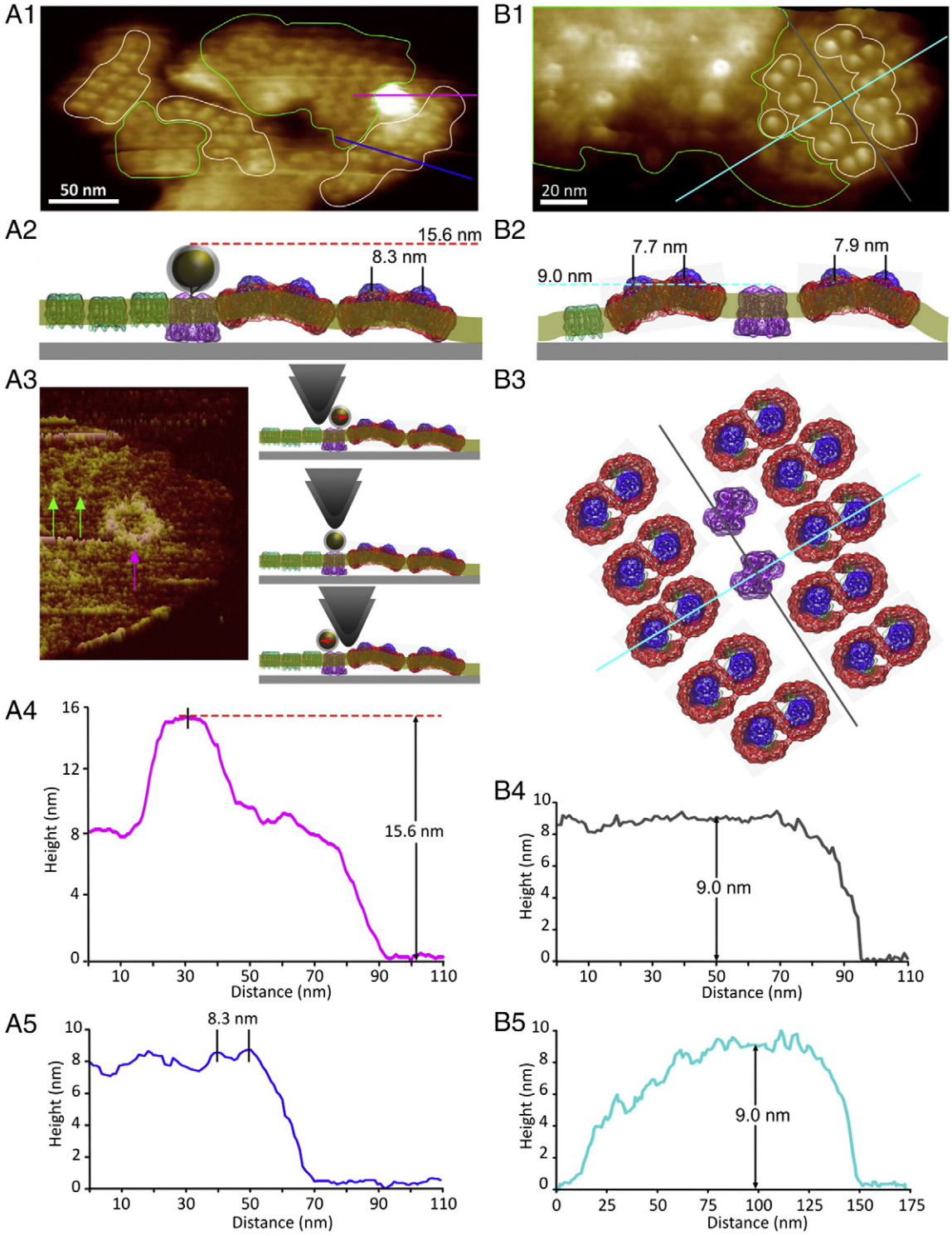

Fig. 5. Comparison of AFM images of a membrane patch containing gold-labelled cytbc_1 complexes and a non-labelled control patch. A1. 3D view of a gold-labelled patch showing the LH2 regions (green outline) and RC–LH1–PufX dimer regions (white outline). The magenta section across the 15.6 nm-high feature (A4) is compatible with a gold bead atop a cytbc_1 complex dimer. The blue section shows the 8.3 nm separation (A5) typical of a core dimer. A2. Model of how the complexes reside in the membrane in relation to the mica surface; the large tip convolution prevents direct visualisation of the complexes adjacent to the putative gold label but both zigzags of LH2 and arrays of RC–LH1–PufX dimers can be seen going underneath this feature. A3. Deformation channel data for the image in A1 showing (left) a clear circular feature (magenta arrow) centred on the maximum height of the high topological feature in Fig. 5A1, and (right) a graphic demonstrating how the sides of the AFM tip would initially displace the gold bead laterally, then tap directly down upon it, then push it aside during the scanning process. B1. 3D view of a non-labelled patch with LH2 and RC–LH1–PufX regions denoted by the green and white outlines; no discrete 15.6 nm-high features were observed for any of the unlabelled membrane patches. B2. Graphic demonstrating the possible co-location of RC–LH1–PufX and cytbc_1, showing the curvature of the membrane and the consequent lack of contact of the complexes with the mica substrate. B3. Model of the membrane in B1, showing how cytbc_1 can be accommodated between rows of RC–LH1–PufX complexes. B4. Section along the area between rows of cores, putatively containing cytbc_1 complexes and corresponding to the grey lines in B1, B3, showing that the cytoplasmic surfaces of the putative proteins are 9 nm above the mica. B5. Section across the area putatively containing cytbc_1 complexes and corresponding to the cyan lines in B1, B3, showing that the patch is not flat on the mica but actually curved, probably as a result of the aligned RC–LH1–PufX complexes which are known to curve the membrane.

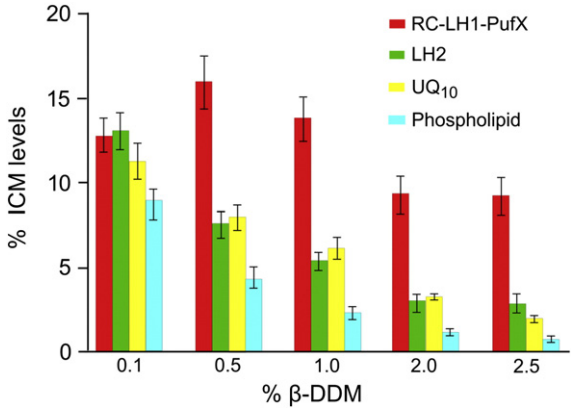

Fig. 6. Selective retention of RC–LH1–PufX complexes following affinity purification of His-tagged cytbc_1 complexes. All cytbc_1, LH2, and RC–LH1–PufX levels are expressed as a percentage of the starting molar ratio of each component per cytbc_1 dimer in the intact membrane (0% β-DDM), as in the first row of Table 1. The error bar is the standard error of the mean. % β-DDM refers to the concentration of detergent used for the initial solubilisation of the membranes (see Materials and methods). All subsequent steps, including washing and elution of the affinity coloumns, were performed with detergent-free buffer.

Table 1
Quantification of the composition of cytbc_1 pulldowns. Rows refer to the molar ratio of a given component per cytbc_1 dimer eluted from each affinity column in detergent-free buffer. Membranes were extracted in triplicate with 0.1, 0.5, 1.0, 2.0, or 2.5% β-DDM, then fractionated using a total of 15 affinity columns. each of the three eluates at a given starting detergent concentration was analysed for complexes or extracted for quinones and lipids in duplicate. The levels of protein complexes in the starting chromatophore vesicles were quantified by mass spectrometry; lipids and quinones were quantified following extraction as detailed in the Materials and methods section. The levels of protein complexes in the affinity column eluates were quantified by absorption spectroscopy, also detailed in the Materials and methods section. The figures in the column are shown with the standard deviation.

Sample	Moles of component per cytbc_1 dimer			
	RC–LH1–PufX dimer	LH2	Total lipids	UQ_{10}
Intact chromatophore	3.4 ± 0.4	21 ± 2.8	4437 ± 677	172 ± 50
0.1% β-DDM	0.43 ± 0.11	2.7 ± 0.7	385 ± 80	19.4 ± 5
0.5% β-DDM	0.54 ± 0.17	1.6 ± 0.5	185 ± 57	13.8 ± 3.8
1.0% β-DDM	0.47 ± 0.15	1.1 ± 0.3	94 ± 32	10.4 ± 3.2
2.0% β-DDM	0.31 ± 0.12	0.60 ± 0.26	46 ± 17	5.5 ± 0.9
2.5% β-DDM	0.31 ± 0.12	0.57 ± 0.37	29 ± 17	3.2 ± 1.1

that are consistent with the 8–10 nm separation distance of RC H-subunits within a RC–LH1–PufX dimer [29]. These AFM images suggest that in these untreated native membrane vesicles of *Rba. sphaeroides* a group of dimeric cytbc_1 complexes sits adjacent to a short array of RC–LH1–PufX dimer complexes.

3.2. Detection of gold-labelled cytbc_1 complexes in membrane patches by electron microscopy and AFM

In order to gain a clearer picture of the distribution of cytbc_1 complexes, with respect to both RC–LH1–PufX and LH2 complexes, we labelled intact chromatophore membranes from the His_{10}-cytc_1 mutant with NiNTA-nanogold, then opened them out using 0.1 mM β-DDM detergent and purified the resulting gold-labelled membrane patches on discontinuous sucrose gradients containing 0.025 mM TDM (see Materials and methods). The EM images of the negatively stained gold-labelled patches (Fig. 4) confirmed the dimeric nature of cytbc_1 complexes and showed that several gold labels appear in a cluster; the larger cluster in Fig. 4F appears to be the sum of the cytbc_1 complexes from two chromatophores, which can be separately counted as five and nine gold labels. This is possibly a result of the tendency of the NiNTA gold beads to crosslink chromatophores by attaching to His–cytbc_1 complexes in initially separate vesicles. Thus, formation of flattened patches from crosslinked vesicles could effectively deplete the number of cytbc_1 complexes, as seen in the upper right patch of Fig 4E, and enhance others (Fig. 4A). Equally, such a membrane patch (Fig. 4A), representing a surface area greater than a single vesicle and with more RC–LH1–PufX, LH2 and cytbc_1 complexes, could have arisen from paired, interconnected vesicles; cryo-electron tomography of plunge-frozen *R. sphaeroides* cells [29] revealed interconnected vesicles, and it is likely that membrane patches prepared from such structures would resemble structures seen in Fig. 4A.

Nevertheless, we can use these patches to gain more information on the location of cytbc_1 complexes. Fig. 4A and B shows the same patch; in Fig. 4A there are two regions of negatively stained larger features on either side of a larger region consisting of smaller circular features that we assign as LH2 complexes. The central membrane zone is clearly the largest, and we assign it to an LH2 domain; the other is RC–LH1–PufX. Our MS analyses indicate that these two complexes, together with cytbc_1, comprise 95% of the membrane proteins present so they also account for the majority of this membrane. Panel B displays a tentative assignment of LH2 complexes (green) and RC–LH1–PufX dimers (red/blue), based on the considerations above, in which gold-labelled cytbc_1 dimers form a cluster adjacent to both the densely-packed LH2 antenna domain and the RC–LH1–PufX dimer arrays. The membrane areas assigned for LH2:RC–LH1–PufX:cytbc_1, taking into account the known sizes of these complexes, are in the ratio 58:37:4. The molar ratios of these complexes were calculated from our proteomic and spectroscopic analyses and, also taking into account their known sizes, the membrane areas for LH2:RC–LH1–PufX:cytbc_1 are predicted to be 52:44:3. Finally, we counted the pixels in Fig. 4A, and the membrane areas (including lipids) assigned for LH2:RC–LH1–PufX:cytbc_1 are 66:25:9. It is interesting to note the agreement between the first two ratios; the largest discrepancy between these two and the third ratio is for the region assigned to cytbc_1, suggesting lipid enrichment in these areas of membrane.

The regions adjoining gold-labelled cytbc_1 were also examined by AFM; the membrane patches are in direct contact with the mica substrate, unlike the upper membrane surface of intact vesicles, so it is possible to make more accurate estimates of the heights and deformation characteristics of the various complexes. Fig. 5A1 shows rows of RC–LH1–PufX dimers, delineated by white lines, and zig-zag areas of LH2 (green lines), which we compare with a typical non-labelled patch imaged to higher resolution, Fig. 5B1. A section across the region of high topology (Fig. 5A1, magenta line) indicates a height of 15.6 nm, consistent with at least one gold nanobead attached to an underlying cytbc_1 complex; see the schematic representation in Fig. 5A2. The four scans prior to that shown in Fig. 5A are displayed in Fig. S2, and demonstrate that this topological feature survives the scanning process whereas a second, membrane-extrinsic feature arising from non-specifically bound surface protein is removed. The non-labelled patch (Fig. 5B2) showed no equivalent discrete high feature and consisted of a curved membrane composed largely of LH2 and RC–LH1–PufX regions. The simultaneously recorded deformation channel for the membrane in Fig. 5A1 produces a clear, circular signal (Fig. 5A3), likely arising from the response of the AFM to lateral movement of the gold nanobead, which is connected to the C-terminus of cytc_1 by a flexible 20-residue linker. Interaction of the scanning AFM probe with peripheral regions of the gold bead and consequent displacement of the bead gives a circular, high deformation signal. In the central region the deformation signal is similar to that of the surrounding protein, consistent with the AFM tip depressing directly down on the nanobead, thus compressing the underlying cytbc_1, as illustrated in the associated cartoon (Fig. 5A3). The position of this central region corresponds to the 15.6 nm topological feature in Fig. 5A1, supporting its assignment as a gold-labelled cytbc_1 complex.

The feature assigned to the cytbc_1 complex in Fig. 5A1 & A3 lies adjacent to a region consisting of LH2 complexes and to an array of paired topological features outlined in white (Fig. 5A1). A section across one of these pairs (Fig. 5A1, blue line, Fig. 5A5) shows a separation of

Table 2
Quantification of RC, cytbc_1, ATP synthase and terminal cytc oxidases within chromatophores by mass spectrometry. Chromatophores were co-solubilised with a ^{15}N-labelled artificial protein standard composed of concatenated sequences of tryptic peptides which are known to represent the target proteins in proteomic analysis. This mixture was subjected to trypsin digestion; each digestion time-point was analysed by nanoLC–MS/MS in duplicate. For each proteotypic peptide, the time-point which gave the highest intensity was used for quantification using the ratio between its (^{14}N) monoisotopic ion and the ^{15}N-labelled counterpart at known concentration. Method details are provided in the Materials and methods section and in Supplementary Information. Although some of the peptides had similar quantification results over two or more time-points, only the highest intensity time-point was used in the final dataset. The final numbers for each proteotypic peptide in the Table are the mean of 2 replicates.

Protein	Tryptic peptide	Quantity (nmol/g total protein)	Stoichio-metry (ratio per 1 PufM)	Stoichio-metry (ratio per 24 PufM)
RC PufM	AEYQNIFSQVQVR	724 ± 1	1.00 ± 0.00	24.0 ± 0.0
RC PufL	ALLSFER	778 ± 112	1.07 ± 0.15	25.8 ± 3.7
Cytbc_1 FbcC	SLSEPGGPELPEDQVR	257 ± 3	0.36 ± 0.00	8.5 ± 0.1
Cytbc_1 FbcF	SVQLGQLVDTNAR	203 ± 14	0.28 ± 0.02	6.7 ± 0.5
ATP synthase AtpF	LAAAEDQIASAEAGAVR	65 ± 9	0.09 ± 0.01	2.1 ± 0.3
ATP synthase AtpX	SDAAAVDAAVAAR	61 ± 2	0.08 ± 0.00	2.0 ± 0.1
ATP synthase AtpA	GIQAAEISAILK	134 ± 6	0.18 ± 0.01	4.4 ± 0.2
	VVDGLGNPIDGK	143 ± 9	0.20 ± 0.01	4.8 ± 0.2
	TAIALDTILNQK	143 ± 1	0.20 ± 0.00	4.7 ± 0.0
Cytc oxidase CoxII	VVSEEAYAAWLEQAR	0 ± 0	0.00 ± 0.00	0.0 ± 0.0
Cytc oxidase CcoO	AQANPDADTDGLLER	31 ± 0	0.04 ± 0.00	1.0 ± 0.0

8.3 nm, consistent with the RC–RC distance measured from the structural model of the dimeric RC–LH1–PufX complex (Fig. 5A2), and with previous AFM data on this membrane-bound complex [29]. Sections across seven of these pairs (Fig. S3) show that they are separated by 7.5 ± 0.8 nm, as reported earlier for core dimers appressed to the mica surface [29], indicating that this region of the membrane adjacent to the gold bead consists of dimeric RC–LH1–PufX complexes. The low resolution and tip convolution effects do not allow us to assess the distances between the surrounding complexes and the cytbc_1. The higher resolution image of the unlabelled membrane (Fig. 5B1) allows the unambiguous assignment of the LH2 region and arrays of dimeric RC–LH1–PufX complexes; additionally the image shows a monomeric core complex immediately adjacent to one row of core dimers. The two core complex arrays surround a zone of limited topology (Fig. 5B4 & B5), which indicates the presence of additional membrane proteins. This region of the membrane is modelled in Fig 5B2 & B3, shown in side and top views, respectively, using measurements taken from the data in Fig. 5B1, together with the crystal structures of the *Rba. sphaeroides* cytbc_1 complex (2QJP) and the core dimer [30]. The model shows that two cytbc_1 complexes can be readily accommodated between the two rows of dimers, and the sections (Fig. 5B4 & B5) demonstrate that the heights measured from the mica to the cytoplasmic surface of the unknown proteins are consistent with the presence of cytbc_1 complexes, probably not fully in contact with the mica substrate. Thus the AFM data on membrane patches are consistent with the EM images in Fig. 4, and with the AFM images of intact untreated chromatophores, Fig. 3A–E, showing that cytbc_1 complexes are found adjacent to RC–LH1–PufX dimer arrays.

3.3. Retrieval of co-purifying complexes using the His-tagged cytbc_1

We sought biochemical evidence for associations between cytbc_1 and RC–LH1–PufX complexes; chromatophore vesicles were partially solubilised by β-DDM detergent, then Ni-NTA affinity chromatography was used to retrieve His-tagged cytbc_1 together with any associated complexes. Increasing concentrations of β-DDM (0.1, 0.5, 1.0, 2.0 and 2.5%) progressively stripped proteins, lipids and quinones from the immediate environment of His–cytbc_1, thereby probing the environment around this complex. The composition of the cytbc_1 pulldown at each initial β-DDM concentration is displayed in Table 2, expressed as moles of each component per mole of eluted cytbc_1 dimer. Absorption spectra of each pulldown are displayed in Fig. S4. The levels of protein complexes in the starting chromatophore vesicles were quantified by mass spectrometry; lipids and quinones were quantified following extraction as detailed in the Materials and methods section. The data in Table 1 and in Fig. 6 show that even the lowest detergent concentration removes approximately 90% of proteins, lipids and quinones, pointing to an unusually detergent-susceptible environment around the cytbc_1. As the solubilising detergent concentration increases there is a tendency for the remaining RC–LH1–PufX complexes to co-purify with cytbc_1, whereas a greater proportion of the LH2 complexes become detached.

3.4. Quantitation of the major membrane protein complexes in chromatophore membranes

In order to build a quantitative structural model of a chromatophore vesicle we used mass spectrometry (MS) to count the number of RC, cytbc_1, ATP synthase, cytaa_3 and cytcbb_3 membrane protein complexes. For this quantitative MS analysis an ^{15}N-labelled internal standard was constructed as an artificial protein composed of concatenated tryptic peptide sequences [13,14] overproduced in *E. coli* and purified on a Ni^{2+}-charged chelating Sepharose column. Chromatophores were mixed with ^{15}N-labelled artificial protein standard and, following digestion, tryptic peptides were analysed in duplicate by nanoflow liquid chromatography coupled to a Maxis UHR-TOF mass spectrometer.

Cytbc_1 complexes were quantified using tryptic peptides from the FbcC (cytc_1) and FbcF (Rieske) proteins; ATP synthase was quantified by its membrane-anchored peripheral stalk subunits AtpF (b) and AtpX (b′) which are present at one copy each per complex [31]. The α-subunit (AtpA), residing in the membrane-extrinsic F_1 sector, occurs in a stoichiometry of 3 per complex [30]. Our observation of a stoichiometry of 4–5 AtpA per chromatophore instead of the 6 expected for two ATP synthases highlights the partial loss of F_1 during chromatophore isolation and demonstrates an advantage, in this case, of using an MS-based determination of the stoichiometry of membrane-anchored proteins over a functional assay. The aa_3 and cbb_3 terminal cytc oxidases were quantified by their CoxII and CcoO subunits, respectively. The former was found to be absent from chromatophores while the cbb_3 cytc oxidase was detected at a copy number of 1. This expression pattern is as expected, given the anaerobic culture conditions used in this study [32]. These results (Table 1) indicate a cytbc_1:RC stoichiometry of 0.28–0.36, equivalent to 3–4 cytbc_1 dimers in a chromatophore containing 24 RCs (see Fig. 7). The ATP synthase has a stoichiometry of 0.08–0.09, relative to the RC, equivalent to 2 complexes per chromatophore.

3.5. Integration of light-harvesting function in a chromatophore vesicle based on an atomic-level structural model

The model of a photosynthetic membrane vesicle combines earlier AFM [6,19], EM [33–35], crystallography [36] and spectroscopy [37] data with the current MS (Table 1), EM and AFM data (Figs. 2–5). This vesicle, adapted from a prior model [17,16], has an inner diameter

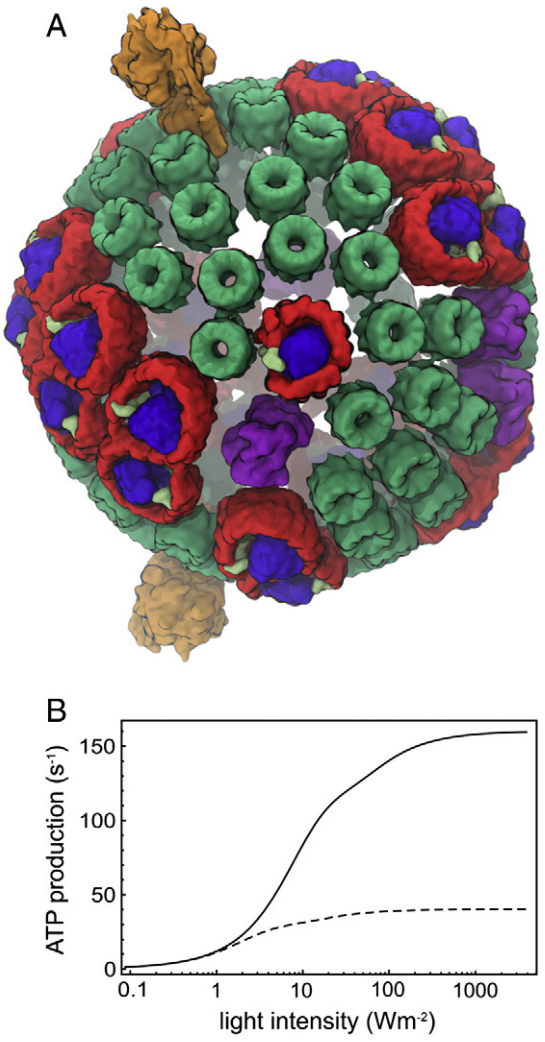

Fig. 7. Atomic structural model of a chromatophore vesicle. A. The vesicle comprises 67 LH2 complexes (green), 11 LH1–RC–PufX dimers & 2 RC–LH1–PufX monomers (blue/red), 4 cytbc_1 dimers (magenta), and 2 ATP synthases (orange) (see movie in Supplementary Information). B. ATP production rate for steady state illumination as a function of incident light intensity for the vesicle shown (solid line) and for a reference vesicle containing only one cytbc_1 dimer complex but 7 additional LH2 complexes to maintain vesicle surface area (dashed line). At a typical low light intensity of 30 W/m^2 the vesicle produces 119 ATP/s, the rate increasing slowly to 158 ATP/s at a saturating intensity of 1 kW/m^2.

of 50 nm and features a 'low light' LH2:RC stoichiometry of 2.7, as well as a packing pattern of LH2 complexes consistent with previous AFM data [19]. Some of the core complexes are monomers, in keeping with biochemical and AFM analyses of photosynthetic membranes [6,38–40]. Fig. 7A displays the model, which comprises the major components of bacterial photosynthesis. Given the delocalisation of proton gradients in the membrane lumen, the exact position of the ATPase is not critical for its function or for our model. The locations of the ATP synthase complexes are assigned tentatively based upon the expectation that they would tend to partition amongst the LH2 complexes, which are of a size and shape similar to those of the membrane-bound F_0 rotor, a cylinder 6 nm tall and 6.2 nm wide [41]. Furthermore, proteomics data suggest a preferential colocation of ATP synthase and LH2 complexes [21]. The four dimeric cytbc_1 complexes are grouped as (2-1-1), giving a RC: cytbc_1 ratio of 3:1, compatible with the quantitative MS analysis (Tables 1 and S1). Extraction data (Table 2) show that such a vesicle would contain ~500–900 quinones, of which 240–360 are sequestered within the dimeric RC–LH1–PufX complexes [11]. A pool of quinones is likely to be closely associated with the immediate environment around core dimers and also around the cytbc_1 complexes, providing a buffer against rapid fluctuations of light intensity, and ensuring robustness of cyclic electron transfer. Associations of two or more RC–LH1–PufX dimers could provide channels for short-range Q/QH_2 quinone diffusion between RC Q_B sites and cytbc_1 complexes [30], contributing to the driving force for the forward reactions in the cytbc_1 catalytic cycle [42].

The primary function of the chromatophore is to capture, transfer, and convert solar energy for ATP production. We used the atomic-level model shown in Fig. 7 to describe the interconnected energy, electron and proton transfer processes in a chromatophore vesicle (see Material and methods as well as a forthcoming publication). For the purposes of this study we assumed that cytochrome c_2 diffusion and ATP/ADP conversion are not rate-limiting sub-processes. A comparison of the turnover rates of constituent proteins indicates that cytbc_1 complexes are rate-determining components at almost all illuminations. To test this assumption we consider a control vesicle containing only one cytbc_1 dimer complex, with 7 additional LH2 complexes compensating for the surface area of the 3 cytbc_1 complexes removed from the model shown in Fig. 7A. Fig. 7B, dashed line, shows that this control vesicle containing only one cytbc_1 dimer can only achieve 37% of the steady-state ATP production rate at a typical low light intensity of 3% full sunlight, compared to a vesicle with 4 cytbc_1 dimers (Fig. 7B, solid line). For the vesicle shown in Fig. 7A the ATP turnover rate is 84–119 ATP/s for light intensities of 10–30 W/m^2 (typical illumination conditions). Such low light conditions (~3% or less of bright sunlight) almost saturate the energy conversion mechanism of the chromatophore; at full sunlight (1 kW/m^2) ATP turnover increases only to 158 ATP/s. Thus, the chromatophore achieves half-maximal ATP turnover already at around 1% of full sunlight, indicating optimal adaptation for low light intensities.

4. Discussion

By using negative stain EM, high resolution AFM, affinity chromatography and quantitative MS we have established the membrane environment and the typical stoichiometries of the cytbc_1 complex in chromatophores of *Rba. sphaeroides* with respect to the RC–LH1–PufX and LH2 complexes and also the ATP synthase. Identification of cytbc_1 required genomic integration of the modified *fbcC* gene, replacing the native gene, to introduce a His_{10}-tag onto the C-terminus of cytc_1. Gold labelling of the tagged complex provided the topology normally absent from the cytoplasmic face of this cytbc_1 complex, and the means to find this complex using AFM. The electron-dense gold label also facilitated identification of cytbc_1 by EM. The EM and AFM data are consistent with cytbc_1 complexes positioned adjacent to RC–LH1–PufX complexes.

Pulldown experiments on chromatophore membranes with His-tagged cytbc_1 as bait (Table 2 and Fig. 6) showed that approximately 90% of the chromatophore protein, lipids and quinones are removed by the lowest concentration (0.1%) of β-DDM detergent. This detergent-susceptible environment could arise from an enrichment of lipids and quinones round the His–cytbc_1 complexes; RC–LH1–PufX complexes sequester up to half the chromatophore quinones (Table 2 and [5,11]), implying quinone enrichment of the local cytbc_1–RC–LH1–PufX membrane environment under steady state illumination conditions as these mobile carriers cycle between the complexes. A quinone-rich phase was proposed to surround the RC–LH1–PufX complexes, on the basis of kinetic data [5]. Approximately 10% of the original RC–LH–PufX complexes retain an association with His–cytbc_1, even in the presence of 2.5% β-DDM, implying a weak but non-stoichiometric interaction between these complexes, rather than a 'hardwired' cytbc_1–RC–LH1–PufX supercomplex of fixed stoichiometry. The small electron transfer domains proposed earlier for *Rba. sphaeroides* [43], are likely to exist, but not as fixed RC–LH1–PufX–cytbc_1 supercomplexes. Instead, cytbc_1 complexes sit adjacent to RC–LH1–PufX complexes in disordered areas likely

caused by the packing mismatch between LH2 and core complexes, with the majority of the RC–LH1–PufX complexes not in direct contact with cytbc_1.

This arrangement might appear to hinder the quinones as they shuttle rapidly between non-adjacent RC–LH1–PufX and cytbc_1 complexes, but the recent structural study of the *Rba. sphaeroides* RC–LH1–PufX complex [30] proposes a channel for quinones to migrate along rows of core dimers. Moreover, imperfect packing of LH2 complexes round the RC–LH1–PufX complexes (see Fig. 7) could create the space for quinone migration along the external faces of RC–LH1–PufX complexes. The dimer structure identified a gap in the LH1 ring adjacent to PufX that allows exchange of quinones and quinols through the LH1 barrier. This work also identified a cavity within the LH1 ring, close to the RC Q_B site [30]. Finally, the structure raised the possibility that quinones can migrate between the two halves of the RC–LH1–PufX dimer, consistent with kinetic data demonstrating quinone sharing by the two RCs within a dimer [5]. These three structural features of the complex could allow rows of core dimers to form channels for quinone diffusion to a nearby cytbc_1 complex. Such an arrangement is depicted in Fig. 7, where three of the cytbc_1 dimers are positioned at the end of two rows of three RC–LH1–PufX complexes. Thus, even 'remote' RC–LH1–PufX dimers are in communication with two or more cytbc_1. Crofts [44] pointed out that, rather than a particular RC having sole access to a dedicated cytbc_1 within a supercomplex, quinols or cytochrome c_2 can visit several cytbc_1 complexes, and this seems likely on the basis of our EM and AFM data.

Another possible consequence of the proximity of cytbc_1 and RC–LH1–PufX complexes is an effective confinement of the extrinsic mobile electron carrier cytochrome c_2, which, as discussed in [1], also must cycle between these complexes to fill the electron hole created by RC photochemistry and enable repeated turnovers of the cytbc_1 complex. In *Rba. sphaeroides* this confinement within the chromatophore interior is enhanced by the tight curvature of the chromatophore vesicle which, if it encloses perhaps 12 cytochrome c_2 molecules, results in a cytochrome c_2 concentration of 0.6 mM. The distances over the internal vesicle surface for diffusion of cytochrome c_2 between the RC and cytc_1 are in the 10–30 nm range, apparently sufficient for cyclic electron transfer.

Although LH2 complexes do not bind or sequester quinone [11], AFM mapping of membranes from an LH2-only mutant of *Rba. sphaeroides* showed that LH2 packing could allow percolation of quinones. There are as many 500 quinones in a chromatophore that are not sequestered by the RC–LH1–PufX complexes; although some of them contribute to a quinone- and lipid-rich phase surrounding the RC–LH1–PufX and cytbc_1 complexes [5] it is possible that the remainder form a more slowly diffusible pool that equilibrates over the whole vesicle on timescales longer than the 1–2 ms required for cyclic electron flow, thus providing a secondary buffer. Such a 'slow' quinone pool could also be important for the function of other complexes such as the cytochrome cbb_3 oxidase, which we found at a level of one per chromatophore (Table 1), but currently we have no information on the membrane location of respiratory chain components.

The chromatophore vesicle represents a membrane surface area of ~7500 nm^2 that apparently partitions to some degree into zones for solar energy collection (LH2), photochemistry (RC–LH1–PufX) and secondary electron transfer (cytbc_1). Thus light-driven cyclic electron flow appears primarily to be sustained by short-range diffusion between cytbc_1 and RC–LH1–PufX complexes, rather than random migration of quinones over the whole chromatophore vesicle. Our proposal parallels the organisation of the equivalent membrane complexes in stacked plant thylakoid membranes, where kinetic studies showed that plastoquinone diffusion between Photosystem II and dimeric cytb_6f complexes is confined within small membrane domains [45], as proposed earlier [43]. With regard to supercomplexes in oxygen-evolving photosynthesising organisms, cytb_6f complexes associate with Photosystem I under conditions that favour cyclic electron flow in *Chlamydomonas* [46,47].

Kinetic models of the chromatophore that account for the interlinked processes of light absorption, energy transfer, electron flow, generation of a protonmotive force and ATP synthesis have been formulated before [25,48]. In this study, we have updated our existing structural model of the chromatophore vesicle [16,17] to take into account the new information on the stoichiometries of the major membrane components and their locations obtained using EM, AFM and MS. We constructed an *in silico* model chromatophore to test the efficiency of this self-contained energy transduction vesicle to produce ATP as a function of illumination. The model clearly demonstrates a robust system that is optimized for the production of ATP under low light illumination, the expected growth conditions for the purple phototrophs such as *Rba. sphaeroides* in a stratified lake. The chromatophore architecture presented above in Fig. 7A, particularly the observed number and organisation of cytbc_1 complexes, optimizes photosynthetic function at low and fluctuating light intensities. The conversion of absorbed energy to ATP appears to be determined by the number of cytbc_1 complexes, as seen in Fig. 7B; cytbc_1 was also identified as the 'kinetic bottleneck' in [25]. We propose that quinone-enriched zones in proximity to the cytbc_1 complexes and the RC Q_B site [11,30,33,34] act as kinetic buffers that smooth the effects of fluctuating light (at sub-second timescales), allowing continuous ATP production during intermittent dark periods. This supramolecular arrangement ensures that quinone diffusion is not rate limiting [5,49]. Therefore, the photosynthetic apparatus displays *robustness* (against rapid fluctuations in light intensity) and *optimality* (of composition for typical growth conditions), thus illustrating adaptiveness, not only at the level of individual proteins as reported earlier [50,51] but also at a system level integration of function.

Author contributions

M.L.C., J.D.O., M.S., P.J.J., A.A.B., and P.Q. designed and performed experiments, M.S. and K.S. did the modelling/computational work, C.N.H., J.D.O., M.L.C., P.J.J., M.J.D., G.J.L., M.S., and K.S. wrote the paper. M.L.C. and J.D.O contributed equally to the work.

Acknowledgements

M.L.C. and G.J.L. were supported by funding from the Engineering and Physical Sciences Research Council, UK (EPSRC, Grant EP/I012060/1). P.Q., P.J.J., A.A.B., J.D.O., M.J.D., and C.N.H. gratefully acknowledge funding from the Biotechnology and Biological Sciences Research Council (U.K.). This work was also supported as part of the Photosynthetic Antenna Research Center (PARC), an Energy Frontier Research Center funded by the US Department of Energy, Office of Science, and Office of Basic Energy Sciences under Award Number DE-SC0001035. PARC's role was to partially fund the Multimode VIII AFM system and to provide partial support for C.N.H. and A.A.B., M.S. and K.S. were supported by the National Science Foundation (MCB-1157615 and PHY0822613) and the National Institutes of Health (9P41GM104601). The authors would like to thank Dr Cvetelin Vasilev, Professor Per Bullough, Elizabeth Martin and David Mothersole for helpful advice.

Appendix A. Supplementary data

Supplementary data to this article can be found online at http://dx.doi.org/10.1016/j.bbabio.2014.02.003.

References

[1] J. Lavergne, A. Verméglio, P. Joliot, Functional coupling between reaction centers and cytochrome bc_1 complexes, in: C.N. Hunter, F. Daldal, M.C. Thurnauer, J.T. Beatty (Eds.), The Purple Phototrophic Bacteria, Springer Netherlands, Dodrecht, 2008, pp. 509–536.

[2] P. Joliot, A. Verméglio, A. Joliot, Evidence for supercomplexes between reaction centers, cytochrome c_2 and cytochrome bc_1 complex in *Rhodobacter sphaeroides* whole cells, Biochim. Biophys. Acta 975 (1989) 336–345.

[3] A. Crofts, M. Guergova-Kuras, S.J. Hong, Chromatophore heterogeneity explains phenomena seen in *Rhodobacter sphaeroides* previously attributed to supercomplexes, Photosynth. Res. 55 (1998) 357–362.

[4] P.R. Rich, Electron and proton transfers through quinones and cytochrome *bc* complexes, Biochim. Biophys. Acta 768 (1984) 53–79.

[5] R. Comayras, C. Jungas, J. Lavergne, Functional consequences of the organization of the photosynthetic apparatus in *Rhodobacter sphaeroides* — I. Quinone domains and excitation transfer in chromatophores and reaction center antenna complexes, J. Biol. Chem. 280 (2005) 11203–11213.

[6] S. Bahatyrova, R.N. Frese, C.A. Siebert, J.D. Olsen, K.O. van der Werf, R. van Grondelle, R.A. Niederman, P.A. Bullough, C. Otto, C.N. Hunter, The native architecture of a photosynthetic membrane, Nature 430 (2004) 1058–1062.

[7] L. Esser, M. Elberry, F. Zhou, C.-A. Yu, L. Yu, D. Xia, Inhibitor-complexed structures of the cytochrome bc_1 from the photosynthetic bacterium *Rhodobacter sphaeroides*, J. Biol. Chem. 283 (2007) 2846–2857.

[8] R. Simon, U. Priefer, A. Pühler, A broad host range mobilization system for *in vivo* genetic engineering: transposon mutagenesis in gram negative bacteria, Bio/Technology 1 (1983) 784–791.

[9] J.H. Roh, S. Kaplan, Genetic and phenotypic analyses of the rdx locus of *Rhodobacter sphaeroides* 2.4.1 [In Process Citation], J. Bacteriol. 182 (2000) 3475–3481.

[10] G. Rouser, S. Fleischer, A. Yamamoto, 2-dimensional thin layer chromatographic separation of polar lipids and determination of phospholipids by phosphorus analysis of spots, Lipids 5 (1970) 494–496.

[11] M. Dezi, F. Francia, A. Mallardi, G. Colafemmina, G. Palazzo, G. Venturoli, Stabilization of charge separation and cardiolipin confinement in antenna-reaction center complexes purified from *Rhodobacter sphaeroides*, Biochim. Biophys. Acta 1767 (2007) 1041–1056.

[12] H. Wang, F. Wang, Z. Wei, H. Hu, Quinone profiles of microbial communities in sediments of Haihe River–Bohai Bay as influenced by heavy metals and environmental factors, Environ. Monit. Assess. 176 (2011) 157–167.

[13] J.M. Pratt, D.M. Simpson, M.K. Doherty, J. Rivers, S.J. Gaskell, R.J. Beynon, Multiplexed absolute quantification for proteomics using concatenated signature peptides encoded by QconCAT genes, Nat. Protoc. 1 (2006) 1029–1043.

[14] J. Rivers, D.M. Simpson, D.H. Robertson, S.J. Gaskell, R.J. Beynon, Absolute multiplexed quantitative analysis of protein expression during muscle development using QconCAT, Mol. Cell. Proteomics 6 (2007) 1416–1427.

[15] E.J. Finehout, J.R. Cantor, K.H. Lee, Kinetic characterization of sequencing grade modified trypsin, Proteomics 5 (2005) 2319–2321.

[16] M.K. Sener, J.D. Olsen, C.N. Hunter, K. Schulten, Atomic-level structural and functional model of a bacterial photosynthetic membrane vesicle, Proc. Natl. Acad. Sci. U. S. A. 104 (2007) 15723–15728.

[17] M. Sener, J. Strumpfer, J.A. Timney, A. Freiberg, C.N. Hunter, K. Schulten, Photosynthetic vesicle architecture and constraints on efficient energy harvesting, Biophys. J. 99 (2010) 67–75.

[18] P.G. Adams, C.N. Hunter, Adaptation of intracytoplasmic membranes to altered light intensity in *Rhodobacter sphaeroides*, Biochim. Biophys. Acta 1817 (2012) 1616–1627.

[19] J.D. Olsen, J.D. Tucker, J.A. Timney, P. Qian, C. Vassilev, C.N. Hunter, The organization of LH2 complexes in membranes from *Rhodobacter sphaeroides*, J. Biol. Chem. 283 (2008) 30772–30779.

[20] J. Hsin, J. Strümpfer, M. Sener, P. Qian, C.N. Hunter, K. Schulten, Energy transfer dynamics in an RC–LH1–PufX tubular photosynthetic membrane, New J. Phys. 12 (2010) 085005.

[21] K. Woronowicz, R.A. Niederman, Proteomic analysis of the developing intracytoplasmic membrane in *Rhodobacter sphaeroides* during adaptation to low light intensity, Adv. Exp. Med. Biol. 675 (2010) 161–178.

[22] J. Strümpfer, M. Sener, K. Schulten, How quantum coherence assists photosynthetic light harvesting, J. Phys. Chem. Lett. 3 (2012) 536–542.

[23] M.K. Sener, J. Strümpfer, J. Hsin, D. Chandler, S. Scheuring, C.N. Hunter, K. Schulten, Förster energy transfer theory as reflected in the structures of photosynthetic light-harvesting systems, Chem. Phys. Chem. 12 (2011) 518–531.

[24] K. Woronowicz, D. Sha, R.N. Frese, R.A. Niederman, The accumulation of the light-harvesting 2 complex during remodeling of the *Rhodobacter sphaeroides* intracytoplasmic membrane results in a slowing of the electron transfer turnover rate of photochemical reaction centers, Biochemistry 50 (2011) 4819–4829.

[25] T. Geyer, V. Helms, Reconstruction of a kinetic model of the chromatophore vesicles from *Rhodobacter sphaeroides*, Biophys. J. 91 (2006) 927–937.

[26] C. Etzold, G. Deckers-Hebestreit, K. Altendorf, Turnover number of *Escherichia coli* F_0F_1 ATP synthase for ATP synthesis in membrane vesicles, Eur. J. Biochem. 243 (1997) 336–343.

[27] D. Mauzerall, The optical cross section and absolute size of a photosynthetic unit, Photosynth. Res. 10 (1986) 163–170.

[28] M. Świerczek, E. Cieluch, M. Sarewicz, A. Borek, C.C. Moser, P.L. Dutton, A. Osyczka, An electronic bus bar lies in the core of cytochrome bc_1, Science 329 (2010) 451–454.

[29] J.D. Tucker, C.A. Siebert, M. Escalante, P.G. Adams, J.D. Olsen, C. Otto, D.L. Stokes, C.N. Hunter, Membrane invagination in *Rhodobacter sphaeroides* is initiated at curved regions of the cytoplasmic membrane, then forms both budded and fully detached spherical vesicles, Mol. Microbiol. 76 (2010) 833–847.

[30] P. Qian, M.Z. Papiz, P.J. Jackson, A.A. Brindley, I.W. Ng, J.D. Olsen, M.J. Dickman, P.A. Bullough, C.N. Hunter, The 3-D structure of the *Rhodobacter sphaeroides* RC–LH1–PufX complex: dimerization and quinone channels promoted by PufX, Biochemistry 52 (2013) 7575–7585.

[31] C. von Ballmoos, A. Wiedenmann, P. Dimroth, Essentials for ATP synthesis by F_1F_0 ATP synthases, Annu. Rev. Biochem. 78 (2009) 649–672.

[32] N.J. Mouncey, S. Kaplan, Oxygen regulation of the *ccoN* gene encoding a component of the cbb_3 oxidase in *Rhodobacter sphaeroides* $2.4.1^T$: involvement of the FnrL protein, J. Bacteriol. 180 (1998) 2228–2231.

[33] P. Qian, C.N. Hunter, P.A. Bullough, The 8.5 Å projection structure of the core RC–LH1–PufX dimer of *Rhodobacter sphaeroides*, J. Mol. Biol. 349 (2005) 948–960.

[34] P. Qian, P. Bullough, C.N. Hunter, Three-dimensional reconstruction of a membrane-bending complex, J. Biol. Chem. 283 (2008) 14002–14011.

[35] T. Walz, S.J. Jamieson, C.M. Bowers, P.A. Bullough, C.N. Hunter, Projection structures of three photosynthetic complexes from *Rhodobacter sphaeroides*: LH2 at 6 Å, LH1 and RC–LH1 at 25 Å, J. Mol. Biol. 282 (1998) 833–845.

[36] G. McDermott, S.M. Prince, A.A. Freer, A.M. Hawthornthwaite-Lawless, M.Z. Papiz, R.J. Cogdell, N.W. Isaacs, Crystal structure of an integral membrane light-harvesting complex from photosynthetic bacteria, Nature 374 (1995) 517–521.

[37] R.N. Frese, C.A. Siebert, R.A. Niederman, C.N. Hunter, C. Otto, R. van Grondelle, The long-range organization of a native photosynthetic membrane, Proc. Natl. Acad. Sci. 101 (2004) 17994–17999.

[38] F. Francia, J. Wang, H. Zischka, G. Venturoli, D. Oesterhelt, Role of the N- and C-terminal regions of the PufX protein in the structural organization of the photosynthetic core complex of *Rhodobacter sphaeroides*, Eur. J. Biochem. 269 (2002) 1877–1885.

[39] E.C. Ratcliffe, R.B. Tunnicliffe, I.W. Ng, P.G. Adams, P. Qian, K. Holden-Dye, M.R. Jones, M.P. Williamson, C.N. Hunter, Experimental evidence that the membrane-spanning helix of PufX adopts a bent conformation that facilitates dimerisation of the *Rhodobacter sphaeroides* RC–LH1 complex through N-terminal interactions, Biochim. Biophys. Acta 1807 (2011) 95–107.

[40] I.W. Ng, P.G. Adams, D.J. Mothersole, C. Vasilev, E.C. Martin, H.P. Lang, J.D. Tucker, C.N. Hunter, Carotenoids are essential for normal levels of dimerisation of the RC–LH1–PufX core complex of *Rhodobacter sphaeroides*: characterisation of R-26 as a *crtB* (phytoene synthase) mutant, Biochim. Biophys. Acta 1807 (2011) 1056–1063.

[41] S. Saroussi, M. Schushan, N. Ben-Tal, W. Junge, N. Nelson, Structure and flexibility of the C-ring in the electromotor of rotary F_0–F_1-ATPase of pea chloroplasts, PLoS ONE 7 (9) (2012) e43045.

[42] A. Osyczka, C.C. Moser, F. Daldal, P.L. Dutton, Reversible redox energy coupling in electron transfer chains, Nature 427 (2004) 607–612.

[43] J. Lavergne, P. Joliot, Restricted diffusion in photosynthetic membranes, Trends Biochem. Sci. 16 (1991) 129–134.

[44] A.R. Crofts, M. Guergova-Kuras, S. Hong, Chromatophore heterogeneity explains phenomena seen in *Rhodobacter sphaeroides* previously attributed to supercomplexes, Photosynth. Res. 55 (1998) 357–362.

[45] H. Kirchhoff, S. Horstmann, E. Weis, Control of the photosynthetic electron transport by PQ diffusion microdomains in thylakoids of higher plants, Biochim. Biophys. Acta 1459 (2000) 148–168.

[46] M. Iwai, K. Takizawa, R. Tokutsu, A. Okamuro, Y. Takahashi, J. Minagawa, Isolation of the elusive supercomplex that drives cyclic electron flow in photosynthesis, Nature 464 (2010) 1210–1213.

[47] H. Takahashi, S. Clowez, F.-A. Wollman, O. Vallon, F. Rappaport, Cyclic electron flow is redox-controlled but independent of state transition, Nat. Commun. 4 (2013) 1–8.

[48] F. Caycedo-Soler, F.J. Rodriguez, L. Quiroga, N.F. Johnson, Light-harvesting mechanism of bacteria exploits a critical interplay between the dynamics of transport and trapping, Phys. Rev. Lett. 104 (2010) 158302.

[49] H. Kirchhoff, U. Mukherjee, H.J. Galla, Molecular architecture of the thylakoid membrane: lipid diffusion space for plastoquinone, Biochemistry 41 (2002) 4872–4882.

[50] M.K. Sener, D. Lu, T. Ritz, P. Park, P. Fromme, K. Schulten, Robustness and optimality of light harvesting in cyanobacterial photosystem 1, J. Phys. Chem. B 106 (2013) 7948–7960.

[51] D. Noy, C.C. Moser, P.L. Dutton, Design and engineering of photosynthetic light-harvesting and electron transfer using length, time, and energy scales, Biochim. Biophys. Acta 1757 (2006) 90–105.